Hybrid Two-Step Inkjet-Printed Perovskite Solar Cells

Raphael Pesch,* Alexander Diercks, Julian Petry, Alexander Welle, Ronja Pappenberger, Fabian Schackmar, Helge Eggers, Johannes Sutter, Ulrich Lemmer, and Ulrich Wilhelm Paetzold*

Perovskite photovoltaics are on their way to commercialization, but crucial advancements are still required to realize scalable and reliable fabrication processes Concerning solution processing of perovskite top solar cells, the hybrid two-step process offers an auspicious combination of good thin-film formation control, even on textures, and high power conversion efficiencies (PCEs). Herein, a scalable fabrication process that consists of a hybrid two-step process and combines evaporated PbI_2 with inkjet-printed organic precursor materials is addressed. It is shown that optimizing the printing parameters enables high PCEs, high reproducibility, and the potential for conformal growth on textured silicon. The perovskite films are free of macroscopic drying effects and omit the use of toxic solvents. To achieve optimal conversion, the morphology of the PbI_2 thin film and the selected resolution in the printing process are decisive. To facilitate intermixing and enable stoichiometry, a dimethyl sulfoxide vapor treatment is introduced to increase the PbI_2 porosity. Reproducible PCEs are demonstrated with champion devices showing 18.2% which are on par with spin-coated counterparts. In the results, it is demonstrated that the hybrid two-step process with an inkjet-printed second step is a promising scalable process for reliable and high-quality perovskite deposition even on texture, thereby paving the path toward industrialization.

1. Introduction

The 2023 report from the Intergovernmental Panel on Climate Change (IPCC) underlines the urgency of reducing carbon dioxide emissions.[1] The IPCC mentions perovskite photovoltaics (PV) among other techniques as one of the key solar energy technologies to further reduce material use per energy produced.[2] Perovskite-based PVs have shown an unprecedented increase in power conversion efficiency (PCE) in the last decade reaching single-junction record PCEs of up to 26.1%.[3,4] Due to their versatile manufacturability[5] and the cost-effectiveness of perovskites as absorber material,[6] perovskite solar cells (PSCs) are considered the next generation of PVs. The ability to adjust their bandgap between 1.2 and 2.3 eV enables the application in tandem PVs in conjunction with established photoactive materials like silicon or CIGS.[7,8] Tandem solar cells based on perovskite-silicon semiconductors achieve the highest certified (non-concentrator) tandem PCEs reaching 33.9%.[4] Despite their high PCEs already demonstrated on a small scale, scalability to large-area solar cells remains a major challenge.[9] There are numerous approaches to the scalability of PSC fabrication, such as evaporation,[10,11] blade-coating,[12,13] slot-die-coating,[14] spray-coating,[15,16] or inkjet printing.[17] Among these technologies, inkjet printing is the only technique that enables free-form processing,[18] minimal material consumption,[19] and precise control of the amount of deposited material. Furthermore, this technology is already established in the industry and has for example been used to produce organic light-emitting diodes.[20] Major challenges of inkjet-printed perovskite solar cells (PSCs) are wetting and crystallization control which lead to high batch-to-batch variation and problems in scalability. These aspects are particularly evident in the one-step processing route, where their control becomes challenging due to the spatially and temporally delayed crystallization process.[21] Additionally, current ink systems for producing highly efficient PSCs within one deposition step are still commonly based on toxic precursor materials such as dimethylformamide (DMF) or n-methylpyrrolidone.[17,22] Using blade-coating for the second step, Siegrist et al. already demonstrated that the implementation of a hybrid two-step deposition process is an effective strategy to omit the reliance on toxic precursor materials and address issues related to scalability and

R. Pesch, J. Petry, R. Pappenberger, J. Sutter, U. Lemmer, U. W. Paetzold
Institute of Microstructure Technology (IMT)
Karlsruhe Institute of Technology (KIT)
Hermann-von-Helmholtz-Platz 1, 76344 Eggenstein-Leopoldshafen, Germany
E-mail: raphael.pesch@kit.edu; ulrich.paetzold@kit.edu

R. Pesch, A. Diercks, R. Pappenberger, F. Schackmar, H. Eggers, J. Sutter, U. Lemmer, U. W. Paetzold
Light Technology Institute (LTI)
Karlsruhe Institute of Technology (KIT)
Engesserstrasse 13, 76131 Karlsruhe, Germany

A. Welle
Institute of Functional Interfaces and Karlsruhe Nano Micro Facility
Karlsruhe Institute of Technology (KIT)
Hermann-von-Helmholtz-Platz 1, 76344 Eggenstein-Leopoldshafen, Germany

reproducibility.[23] Instead of dissolving the lead iodide into toxic precursor materials, this approach resorts to vapor deposition as a first step. While the possibility of a two-step deposition of the perovskite thin film has been recognized for more than two decades,[24] this method has risen in popularity in perovskite PV within recent years due to the good reproducibility of high-quality perovskite thin films and record efficiencies.[25,26] However, highly efficient hybrid two-step fabricated PSCs have so far mainly been demonstrated for non-scalable methods, or using blade-coating.[23,26,27] Initial studies showed that by using inkjet printing instead of blade-coating in the second step, the overall homogeneity of the perovskite is greatly improved, although multiple crossings of the print head result in millimeter-sized stripes forming in the perovskite.[28] In this work, we investigate the specific challenges for hybrid two-step fabricated PSCs based on inkjet printing and present solutions to overcome them. We show that the choice of printing parameters influences not only the stoichiometry but also the formation of inhomogeneities within the perovskite layer due to printing patterns. In answer to this, we propose a general approach to reduce these inhomogeneities. Using a fixed ink system, we demonstrate that for each subsequent lead iodide thin film only one ideal printing resolution occurs. We optimize the inkjet-based hybrid two-step process by introducing an additional dimethyl sulfoxide (DMSO) evaporation step between the two deposition steps and show that PSCs based on evaporated lead iodide thin films can perform similarly well as PSCs based on liquid-processed lead iodide thin films with remarkably high batch-to-batch reproducibility. Finally, this work demonstrates the advantages of an inkjet-based hybrid two-step process for the deposition of conformal perovskite thin films on textured silicon substrates.

2. Results and Discussion

2.1. Tuning the Lead Iodide Thin-Film Morphology

To the best of our knowledge, as of now, there are no reports on the interdiffusion process of sequentially deposited perovskite materials and the influence of the morphology of the evaporated lead iodide thin film when inkjet printing is used as the second step. The sequential nature of material deposition in the two-step process, illustrated in **Figure 1**, underscores the significance of material diffusion for achieving a complete and homogeneous perovskite conversion. Consequently, it is necessary to enhance diffusivity, for instance, by increasing porosity, to ensure the formation of a perovskite thin film with optimal homogeneity throughout the perovskite. To investigate the influence of differently deposited lead iodide thin films on the formation of hybrid two-step deposited perovskites using inkjet printing as a second step, a liquid-processed (spin-coated) and a vapor-processed (thermally evaporated) lead iodide thin film are compared. Furthermore, the same properties are determined for a vapor-processed lead iodide thin film that is subsequently exposed to DMSO vapor. In a previous study, Xiao et al. highlighted the advantageous impact of a vapor-assisted solution process.[29] However, their approach involved the utilization of DMF, resulting in an extended evaporation period lasting several hours. Furthermore, they applied the vapor treatment at the concluding annealing stage of the overall perovskite fabrication process instead of employing it to modify the lead iodide thin film. Subsequently, Chen et al. showed that by using DMSO the treatment time is remarkably reduced to a mere few minutes.[30] Both Xiao et al. and Chen et al. demonstrated the positive effects of an additional solvent vapor treatment exclusively on spin-coated lead
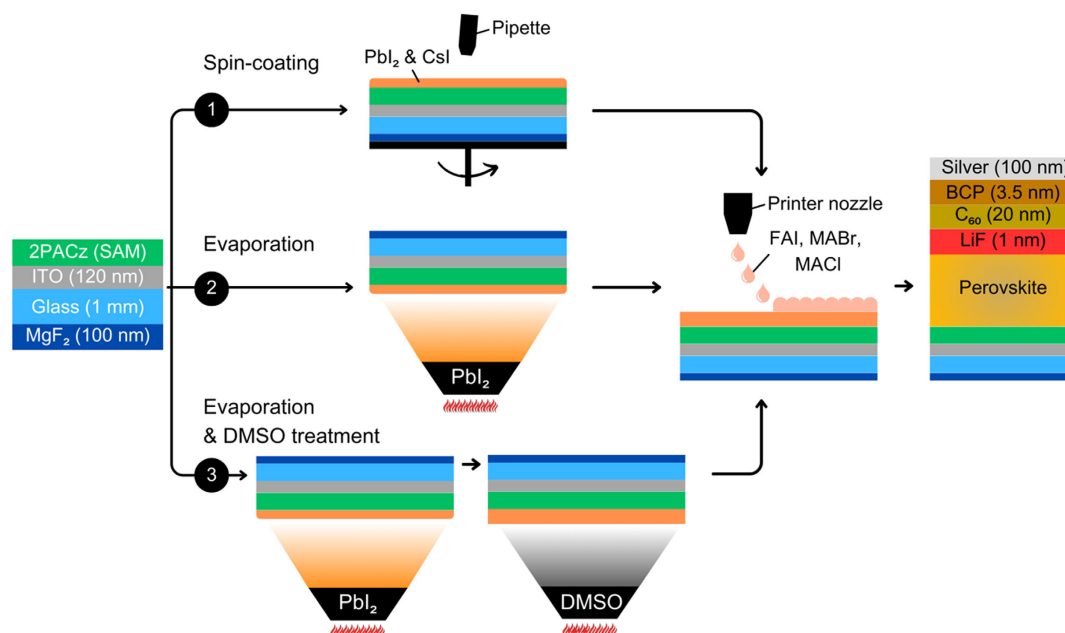

Figure 1. Manufacturing process of PSCs using a (hybrid) two-step deposition method combining either spin-coating or evaporation with inkjet printing.

iodide thin films or perovskites based on spin-coated lead iodide thin films. A study by Nguyen et al. introduced this supplementary treatment step on evaporated lead iodide thin films.[31] Their findings indicated that such treatment enhances the conversion process when employing blade-coating as the second step in a hybrid two-step perovskite deposition method. It is noteworthy that even a brief treatment of the lead iodide thin film forms a considerably more porous lead iodide thin film.

Using scanning electron microscopy (SEM) and time-resolved microscopy (PicoDrop drop-watcher setup), the influence of the porosity on the absorption of the organic cation precursor into the lead iodide thin film is investigated. As suggested by literature,[32,33] the SEM images indicate that the spin-coated lead iodide thin film is considerably more porous than the evaporated one. This property leads to an increased absorption of the subsequently deposited organic cation precursor as shown by time-resolved microscopic photographs of droplets (around 30 pL) on the respective lead iodide thin film. As shown in **Figure 2**, droplets of the organic cation precursor are completely absorbed by the spin-coated lead iodide thin film within 1.9 s. In contrast, the droplets deposited onto the pristine-evaporated lead iodide thin films remain on the surface without being fully absorbed (Figure 2b). However, for the DMSO-vapor-treated evaporated

lead iodide thin film, the absorption time is considerably decreased (1.3 s) compared to even the spin-coated lead iodide thin film (Figure 2c). We propose, that this is related to the increased porosity of the lead iodide thin film. While the droplet absorption does not per se equal the diffusivity of the entire lead iodide thin film, it is expected that it strongly correlates to the diffusion of the organic cation precursor into the lead iodide thin film. Time-of-flight secondary ion mass spectrometry (ToF–SIMS) measurements carried out in this work (Section 2.4) confirm this assumption.

As also observed by Nguyen et al. X-ray diffraction (XRD) measurements indicate that the vapor pretreatment with DMSO not only changes the morphology of the lead iodide thin film but also incorporates DMSO into it (Figure 2). Furthermore, we hypothesize that the micrometer-sized formations are lead iodide–DMSO complexes, which according to Nguyen et al. are more porous than pristine-evaporated lead iodide. Compared to the pristine-evaporated lead iodide thin film, the characteristic DMSO complex peak at 9.94° can be seen in the XRD measurements. This peak is similarly observed at the identical 2θ angle in the XRD measurements of the lead iodide thin film produced by spin-coating. For a similar DMSO evaporation setup as used by Nguyen et al. we find
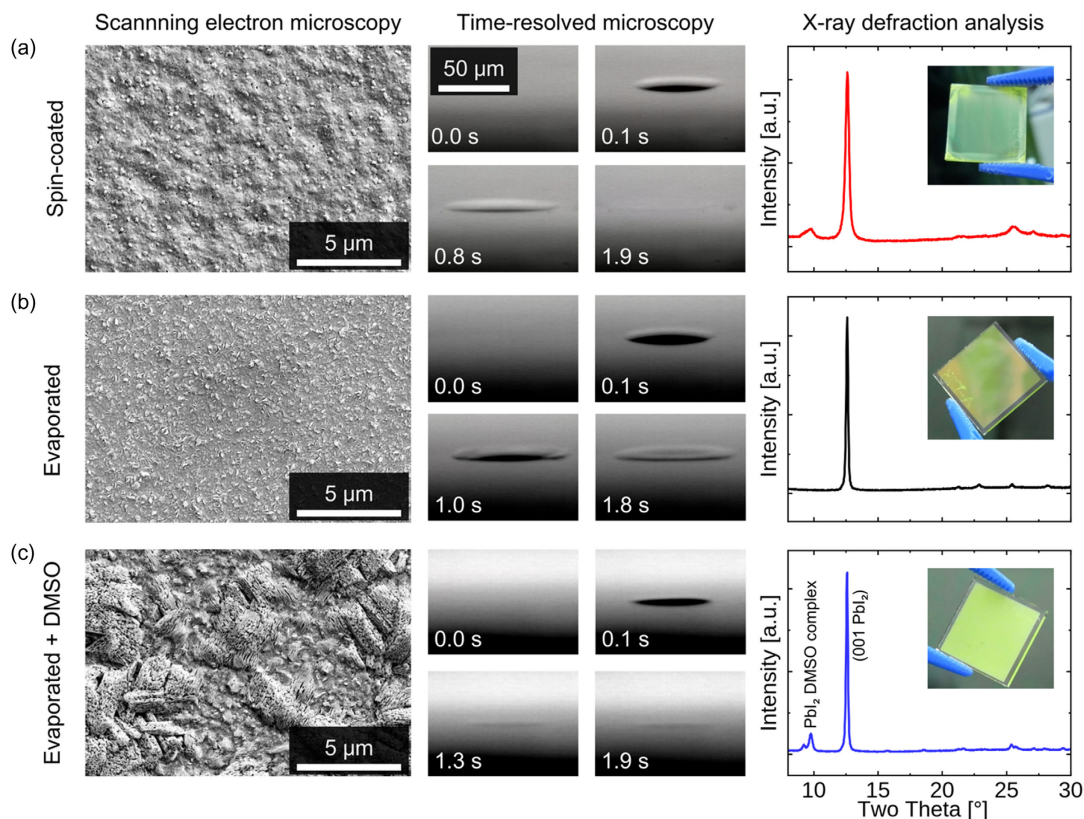

Figure 2. Lead iodide morphology, crystallinity, and absorption depending on the deposition process. Shown for a) spin-coated, b) evaporated, and c) evaporated DMSO-vapor-treated lead iodide thin films. The absorption properties can be seen from time-resolved microscopy (PicoDrop drop-watcher setup), SEM images' morphology, and XRD measurements' crystallinity. The PicoDrop images show the different interaction types (absorption and surface pinning) of the organic cation precursor with the differently deposited lead iodide thin films. Compared to evaporated lead iodide thin films, both the spin-coated and the DMSO-vapor-treated evaporated lead iodide thin films show increased absorption of the organic cation precursor.

identical evaporation times (30 s with an 80 °C hot plate) as Nguyen et al. for the optimal perovskite conversion. However, to enhance the reproducibility of this pretreatment step the DMSO evaporation parameters are changed. Hereby, the hot plate temperature is changed to 60 °C which resulted in a longer, more reproducible evaporation time of 40 s. With this longer evaporation time, we achieve similar results on the 80 °C hot plate.

2.2. Suppressing Printing Patterns

Inhomogeneous material deposition and conversion that result in stripe-like printing patterns along the printing direction are known artifacts that appear in hybrid two-step processed perovskite thin films with inkjet-printed organic cation precursors.[28] Macroscopic drying effects are a known hurdle when it comes to one-step inkjet printing or other scalable liquid deposition methods like spray-coating. They need complex iterative ink engineering to be circumvented.[21] Here, we show that drying-related printing patterns can be circumvented by increasing the deposition time of adjacent droplets and optimizing the organic cation precursor. Unless otherwise mentioned, the following optimization was carried out with a printing resolution of 1000 droplets per inch (DPI). The influence of different DPIs and the reasons for choosing 1000 DPI are addressed in Section 2.4. Due to the previously discussed preferred absorptive property of porous lead iodide thin films, we know that adjacent droplets require enough time (>1 s), to be completely absorbed. We hypothesize that macroscopic drying effects mainly occur when droplets fuse and form a wet film that eventually underlies drying processes such as the coffee-ring effect or the Marangoni effect.[34,35] Photoluminescence mappings of perovskites printed with different deposition times of adjacent droplets support this assumption. While photoluminescence mappings of perovskites printed with adjacent-droplet deposition times of milliseconds show macroscopic drying effects (**Figure 3**a), counterparts fabricated with droplet deposition times perpendicular to the direction of print head travel of more than 1 s, appear more homogeneous (Figure 3b). Generally, two printhead configurations can be used to achieve a given resolution: printing with a variable printhead angle or with a fixed angle, so-called native

printing. To achieve high printing resolutions, at which adjacent droplets have a smaller distance than adjacent nozzles, in native printing the printhead needs to cross the substrate several times. As such, this configuration is more time-consuming compared to its counterpart angled printing. However, our work uses this effect to enable better absorption of individual droplets before printing their adjacent droplets. The ability to prevent macroscopic drying effects by simply printing with a native print head configuration is a major benefit. An advanced setting that some inkjet printers offer beyond that is the possibility to individually control the deposition of each nozzle. Hereby, the deposition of, e.g., every nth droplet within one crossing can be left out and filled up using another nozzle when the print head crosses the substrate again. In the following, the number of droplets to be left out by a nozzle in the direction of print head travel is called the vertical step size (SS_V). Similarly, it is possible to leave out droplets perpendicular (horizontal step size [SS_H]) to the direction of print head travel. In addition to an increased deposition time of adjacent droplets, choosing $SS_V > 1$ and $SS_H > 1$ has the benefit of printing an area of SS_V by SS_H in pixels without using a nozzle twice. This reduces the probability of pinholes due to the clogging of one nozzle. Droplet deposition sequences that occur for different SS_V and SS_H combinations are visualized in Figure S1, Supporting Information. In addition to an improved overall homogeneity compared to only natively printed perovskites, combining native printing with a moderate SS_V (=3) and SS_H (=3) further suppresses macroscopic drying effects and leads to blur-free, sharp print edges (Figure 3c). Increasing the SS_V and SS_H even more, the photoluminescence mapping shows macroscopically improved homogeneity. However, small drying patterns appear once the SS_V and SS_H are increased to values greater than or equal to $SS_V = 8$ and $SS_H = 8$ (Figure 3d). Microscope images reveal that these patterns originate from single droplets. We assume these droplets have too much time before a droplet is deposited next to them. The alcohol in the ink completely evaporates before an adjacent droplet is deposited. Without remaining alcohol, a droplet cannot connect with its adjacent droplet inside the lead iodide thin film. A stepwise reduction of the molarity of the organic cation precursor from 0.5 to 0.17 M strengthens this assumption since the microscopic drying effects are eliminated with lower molarities
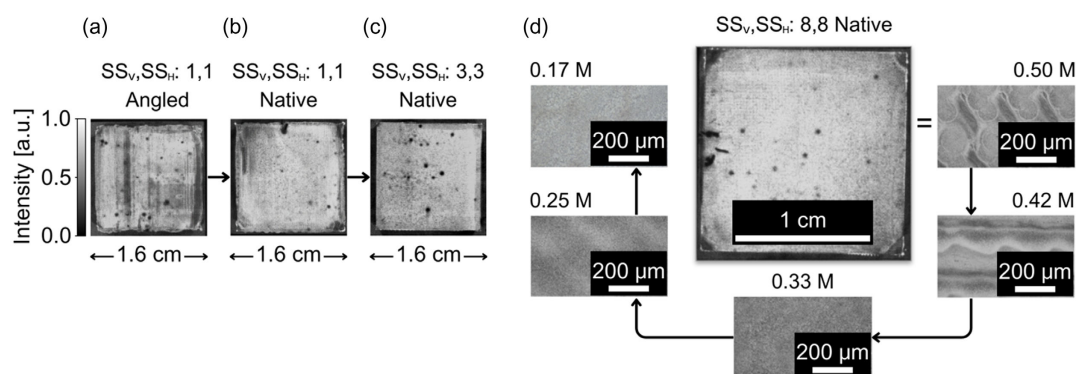
Figure 3. a–d) Photoluminescence mappings of perovskites produced with different print head arrangements (angled/native), vertical step sizes (SS_V, direction of print head travel), and horizontal step sizes (SS_H, perpendicular to the direction of print head travel). d) Influence of different molarities of the organic cation precursor on the homogeneity of the final perovskite analyzed with microscope images.

(Figure 3d). However, to still be able to provide enough organic cations while lower molarities are used, more droplets are needed. A reduction of the molarity from 0.5 to 0.17 M, for example, necessitates an increase from 1000 to 1732 DPI. This however increases the printing time even further. The comparison of the electrical parameters from PSCs printed with high SS values ($SS_V = 10$, $SS_H = 10$) versus moderate SS values ($SS_V = 3$, $SS_H = 3$), as well as PSCs printed with different molar organic cation precursors and printing resolutions, shows limited influence in the investigated range (Figure S2 and S3, Supporting Information). Hence, we propose limiting the SS values and ink molarity to a maximum of $SS_V = 3$, $SS_H = 3$, and a minimum of 0.5 M.

2.3. Revealing the Material Distribution throughout the Perovskite Thin Film

Using ToF–SIMS measurements, we show that an improved material distribution throughout the perovskite occurs if the inorganic thin film is subjected to a DMSO vapor treatment. In addition to that, we show the formation of an HTL-attached remaining lead iodide thin film for low printing resolutions and an increased strip formation in case of high printing resolutions. Depth-integrated x–y images reveal that the perovskite based on the spin-coated lead iodide thin film shows a stripe-like printing pattern (**Figure 4**a). In contrast, the perovskite thin film based on an evaporated lead iodide thin film appears homogeneous. Once the evaporated lead iodide thin film is DMSO-vapor-treated, printing patterns in the form of droplets occur. Height profile measurements reveal that the x–y inhomogeneities mainly arise from the height profile of the stripes (Figure S4, Supporting Information). Interestingly, the printing patterns also appear within the depth-integrated x–y images of the PbI^+, indicating that the alcohol of the organic cation precursor solution can transport the lead iodide once it contains DMSO complexes. This suggests that intermixing is improved when DMSO-lead iodide complexes are present. A simplified schematic in Figure 4a visualizes the suggested underlying processes that occur when DMSO is introduced. x–y-integrated depth profiles (z-direction) reveal that, under optimal stoichiometry, a sufficient amount of organic cations reach the HTL, thereby preventing the formation of a pristine lead iodide layer near the HTL (Figure 4a). The $(PbI^+/FA^+)_{noDMSO}$ to $(PbI^+/FA^+)_{DMSO}$ ratio enables a comparison of the FA^+ incorporation of both perovskites based on evaporated lead iodide in the z direction. As a result of this, a value >1 indicates a locally higher FA^+ amount within the perovskite which is based on DMSO-vapor-treated evaporated lead iodide. Since the ratio not only shows values above one but also increases along the perovskite depths, a better FA^+ incorporation is to be expected for the perovskites based on DMSO-vapor-treated lead iodide (Figure S5a, Supporting Information). Height measurements show that the perovskite based on the spin-coated lead iodide thin film is ≈150 nm thicker than the perovskite based on the evaporated lead iodide thin film (Figure S6, Supporting Information). This trend is also confirmed by ToF–SIMS measurements, since for perovskite thin films based on a spin-coated lead iodide thin film, almost twice the number of ions per square centimeter are necessary to erode

the perovskite. The hypothesis that for a given organic cation precursor the printing resolution determines the stoichiometry is validated by the ToF–SIMS measurements. The lead iodide thin film is not converted entirely for printing resolutions below the optimum of 900 DPI, resulting in a sub-stoichiometric composition of the perovskite (Figure 4b). Furthermore, residual pristine lead iodide remains. The depth profiles through the perovskite reveal that the remaining lead iodide is located on the HTL. In the case of excess organic cations, depth-integrated x–y images show strong inhomogeneities in the material distribution, which follows a stripe-like printing pattern. Once again, height profile measurements reveal that they stem from variations in the perovskite thin-film height rather than from compositional inhomogeneities (Figure S4, Supporting Information). Interestingly, the height variations only appear when the optimal printing resolution is exceeded. The $(PbI^+/FA^+)_{1100\,DPI}$ to $(PbI^+/FA^+)_{900\,DPI}$ ratio shows a value >1 for all depths (see Figure S5b, Supporting Information). Therefore, the excess cations are distributed through the whole perovskite forming an over-stoichiometric perovskite throughout the thin film. A simplified schematic in Figure 4b visualizes the detected and previously described material distribution for the three different stoichiometries.

2.4. Connection between Inkjet Printing Parameters and PSC Performance

Similar to the morphology of the lead iodide thin film, printing parameters play a crucial role in the hybrid two-step process to produce high-quality perovskites. In addition to revealing that the ideal stoichiometry is contingent upon the printing resolution, the study illustrates the impact of both an excess and a deficiency of organic cations on the electrical properties. Determining the optimal amount of organic cations becomes crucial considering the fixed quantity of lead iodide. All materials applied during the inkjet-printing process contribute to the final perovskite thin film, requiring a stoichiometric match with the lead iodide thin film. Due to the unknown porosity and, therefore, density of the lead iodide thin film, calculating the amount of organic cation precursor needed for a stoichiometric perovskite conversion is challenging. Using inkjet printing there are three ways to experimentally determine the stoichiometric optimum by changing the amount of material deposited. The first option is to vary the droplet size. However, this hardly plays a role in practice since one print head is only designed for one droplet size. The second option is to change the molarity of the organic cation precursor. In this work, we propose a 90% v/v n-butanol 10% v/v isopropyl alcohol (IPA) mixture to dissolve the organic cations instead of pure IPA as commonly used in literature.[7,23,31] We use this ink composition due to the higher viscosity and surface tension of n-butanol to guarantee stable jetting. As seen in (Figure S7, Supporting Information), PSCs processed with 100% IPA as ink solvent versus 100% n-butanol as ink solvent showed similar electrical properties. The organic cation precursor used in this work is based on a widely used two-step recipe[36,37] containing 60 mg mL^{-1} formamidinium iodide (FAI), 6 mg^{-1} methylammonium bromide (MABr), and 6 mg mL^{-1} methylammonium chloride (MACl), corresponding to a 0.5 M ink. This recipe results
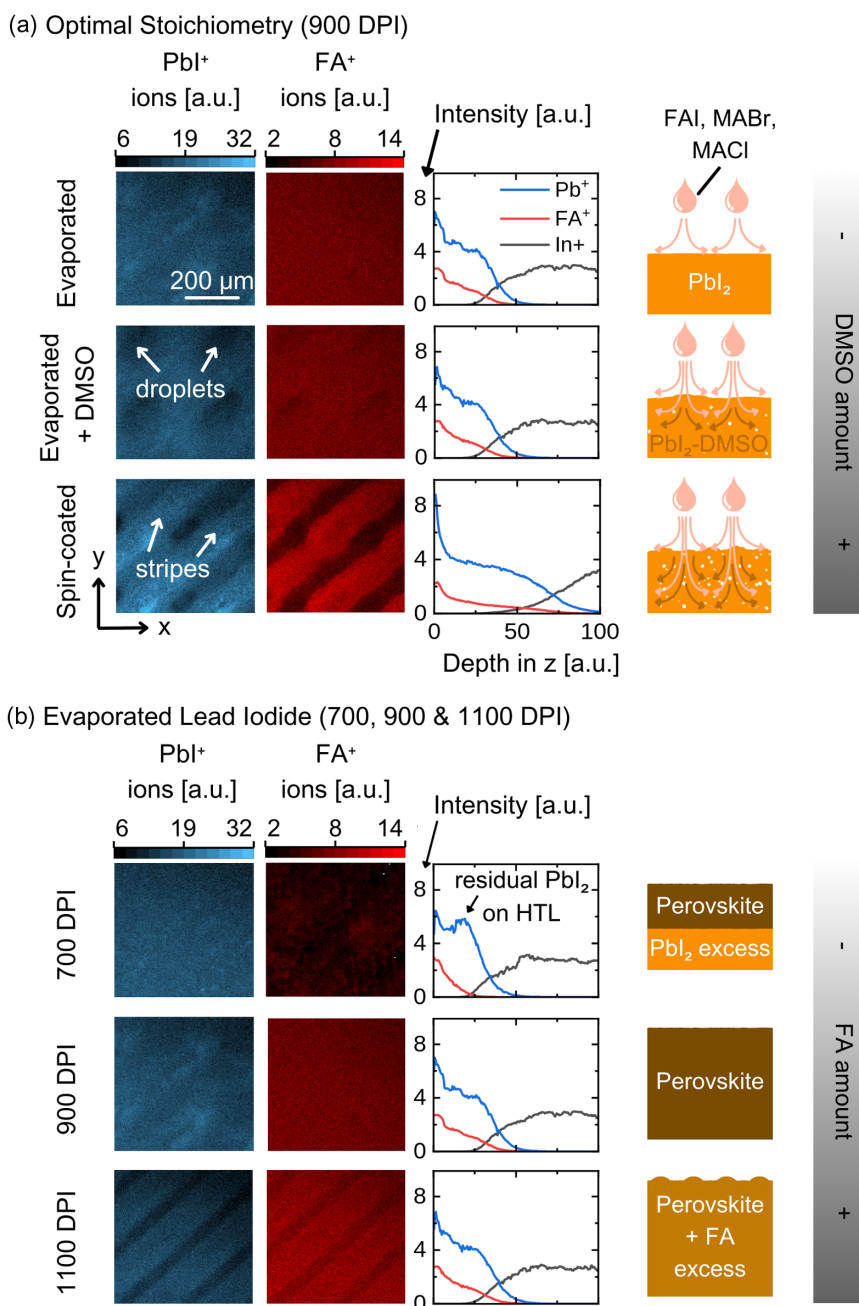
Figure 4. ToF–SIMS measurements: Depth-integrated x–y images and x–y-integrated depth profiles revealing the material distribution of the inorganic lead iodide (represented by $^{206/207}$PbI$^+$ or ^{208}Pb$^+$ cations) and the organic cations (represented by the dominating FA$^+$ cations, detected as ^{13}CH$_5$N$_2$$^+$) within the annealed perovskite thin film. a) Comparison of the material distributions for the optimum stoichiometry (900 DPI) between perovskites based on evaporated, DMSO-vapor-treated evaporated, and spin-coated lead iodide thin films. A schematic below the ToF–SIMS images visualizes the assumed underlying processes. b) Comparison of the material distributions for perovskites based on evaporated lead iodide thin films below (700 DPI), at (900 DPI), and above (1100 DPI) the optimum stoichiometry. A schematic besides the ToF–SIMS images visualizes the material distribution for the three stoichiometric cases. Within all graphs, blue represents lead iodide (detected as $^{206/207}$PbI$^+$ or ^{208}Pb$^+$), red represents the organic cations (detected as ^{13}CH$_5$N$_2$$^+$), and black represents the ITO layer (detected as ^{113}In$^+$). The depth-correlated fluence represents the depth of the perovskite thin film.

in a stoichiometry Cs$_{0.05}$MA$_{0.28}$FA$_{0.67}$Pb(Br$_{0.03}$Cl$_{0.06}$I$_{0.91}$)$_3$ for the perovskite thin films based on the spin-coating technique. The composition is determined based on the chosen molarity of the lead iodide solution (in the case of spin-coating), or the molar mass and layer thickness of the lead iodide layer

(in the case of thermal evaporation), as well as the known mass ratio of the A site cations and X site halides, used in the second step. To determine the composition, it is assumed that the underlying perovskite is in the ideal (ABX$_3$) stoichiometry. Higher molarities than 0.5 M are also investigated but are

**ADVANCED
SCIENCE NEWS**

www.advancedsciencenews.com

Solar
RRL

www.solar-rrl.com

impractical because they can only be dissolved in n-butanol after very long mixing times and precipitate again within hours. As mentioned in Section 2.2, lower molarities are considered for homogeneity optimization but require high printing resolutions, which therefore result in longer printing times. Lastly, the amount of material deposited can be varied by changing the printing resolution measured in droplets per inch (DPI). For a linear increase in resolution, the amount of material deposited increases quadratically. For the lead iodide thin films used in this work (produced by evaporation and spin-coating), 1000 DPI is experimentally determined as the optimum when using a 10 pL print head. It should be mentioned that this value can vary slightly between each batch since a possible batch-to-batch fluctuation of the lead iodide thin-film height influences the amount of the needed organic cation precursor. Since the evaporated lead iodide thin films are 300 nm in height while the spin-coated thin films are 500 nm in height, both show the best performance using 1000 DPI. This further indicates the different porosity of the lead iodide thin films.

Figure 5 shows the performance of the PSCs processed with a two-step process and variable DPI of the inkjet-printed organic cation precursor. Starting from 700 DPI, the median PCE increases from 11% to 17% once it reaches 1000 DPI. Increasing the DPI further, the median PCE decreases more rapidly, reaching 11% again for 1100 DPI (Figure 5a). We conclude that a lack of organic cations decreases the device's performance less than an excess of organic cations. Up to the tipping point of 1000 DPI, the gain in PCE with increasing DPI is mainly attributed to the increasing fill factor (FF) and short-circuit current density (J_{SC}), which are displayed in Figure 5b,c, respectively.

ToF–SIMS measurements suggest that the HTL-attached remaining lead iodide thin film, which is decreasing with increasing DPI, is the origin of this trend. Increasing the DPI leads to a strong increase in the external quantum efficiency (EQE) across the entire spectrum, particularly for wavelengths shorter than the bandgap of lead iodide (2.35 eV ≈ 528.5 nm) (Figure 5e). The integrated photocurrents match with the measured J_{SC} values and therefore strengthen the mechanism proposed earlier (Figure S8, Supporting Information). In conclusion, the absorption of photons above the lead iodide's bandgap and the prevalent recombination of generated electron–hole pairs within the lead iodide contribute to a decrease in the EQE for lower DPI. As further mentioned in Section 2.3, height profile measurements (Figure S4, Supporting Information) reveal that for higher DPIs the thickness of the perovskite increases. This ensures an increased effective light pathway length and, according to the Beer–Lambert law, an increased overall absorption. Using the one-step deposition, EQEs of up to 90% for photon energies larger than the bandgap of lead iodide can be achieved.[38] Similar EQEs can also be reached with the two-step approach used in this work (Figure 5e). Next to the J_{SC}, the FF correlates to the composition of the perovskite absorber (Figure 5b). It increases linearly up to the optimum DPI and strongly drops after exceeding it. While a negative deviation of 200 DPI from the optimal printing resolution results in a loss of less than 10% in the median FF, the same deviation toward a higher printing resolution means a loss of more than 25% in the median FF. This observation arises because, in comparison to the optimum DPI, the series resistance increases significantly for lower resolutions. For higher resolutions than the
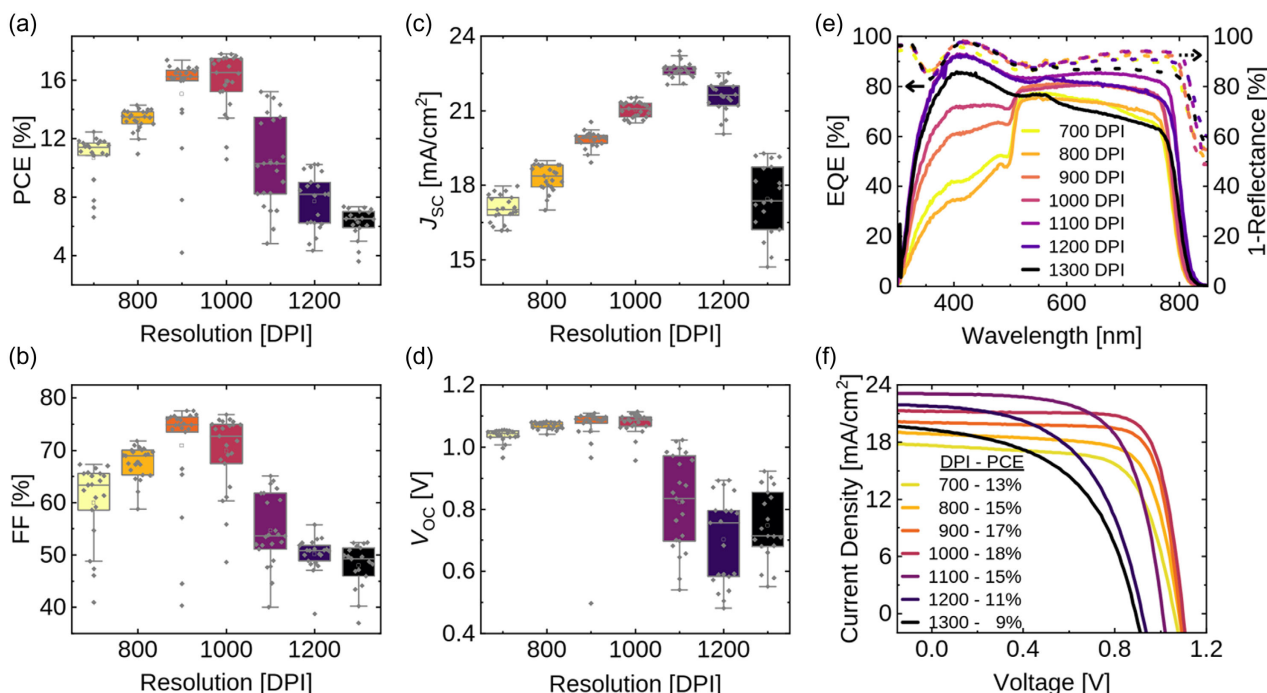

Figure 5. Influence of different resolutions on the electrical parameters of hybrid fabricated inkjet-printed PSCs. a–d,f) The electrical properties (PCE, FF, J_{SC}, V_{OC}, and J–V curve) over the DPI. e) The absorptance (1-R) and the EQE for different DPIs. Figure S8, Supporting Information, shows the integrated current densities that belong to the EQEs in (e).

optimum DPI, both series resistance and shunt resistance deteriorate (Figure 5f). As discussed by Liu et al. this observation can be explained by pinholes introduced into the perovskite absorber with an organic cation excess.[39] Interestingly, the open-circuit voltage (V_{OC}) (Figure 5d) remains nearly independent of the DPI below the optimal DPI, exhibiting a slight increase as the DPI rises. ToF–SIMS measurements carried out within this work (Section 2.3) show that the observed slight increase in V_{OC} correlates to the stepwise reduction of remaining lead iodide with increasing DPI. We hypothesize that the voltage drop occurs across the HTL-attached lead iodide thin film. Compared to the slight increases in V_{OC} toward the optimal DPI, the V_{OC} decreases significantly once surpassing the optimal DPI. Even for half of the amount of organic cation precursor compared to the optimum DPI (700 vs 1000 DPI), less than a tenth of a volt gets lost regarding the median V_{OC}. Once reaching 1100 DPI, the median V_{OC} immediately decreases by a few tenths of a volt, which, according to the results of Liu et al. might be caused by pinholes.[39] This assumption would furthermore explain the strong V_{OC} spread occurring. Together with FF, after surpassing the optimum DPI, the drop in V_{OC} significantly reduces the PCE. The decrease in PCE cannot be compensated by the further increasing J_{SC} at 1100 DPI and is intensified by the drop in J_{SC} for even larger DPI. The properties depicted here apply not only to PSCs based on the spin-coated lead iodide thin films but also to those based on the evaporated lead iodide thin films (Figure S9, Supporting Information).

2.5. Potentials of Hybrid Two-Step Deposition Using Inkjet Printing

The lead iodide deposition method, and particularly an additional DMSO vapor pretreatment of the evaporated lead iodide thin films, strongly influences the performance of the processed PSCs. Interestingly, the PSCs based on spin-coated lead iodide perform the best, even though ToF–SIMS revealed that it shows the highest inhomogeneity in the x–y plane, as well as in the x–z plane compared to the PSCs based on evaporated lead iodide (Figure S10, Supporting Information). We, therefore, conclude that the avoidance of inhomogeneities appears to be less important. Since another already noted difference between the PSCs based on spin-coated and evaporated lead iodide is the total height of the final perovskite, we furthermore conclude that a thicker perovskite is beneficial. However, since the interdiffusion into evaporated lead iodide thin films is harder to achieve, increasing the thickness is only useful to a certain extent. Champions devices exhibit PCEs, determined by current density–voltage (J–V) measurements of 19% for a PSC based on a spin-coated lead iodide thin film, 16.7% for a PSC based on a pristine-evaporated lead iodide thin film, and 18.2% for a PSC based on an evaporated and DMSO-vapor-treated lead iodide thin film (**Figure 6**a). It should be noted that all PSCs show EQEs of up to 90% which suggests good conversion (Figure 6c). In comparison to fully spin-coated similar bandgap two-step triple-cation PSCs, which achieve PCEs of up to 20%, switching to scalable deposition methods is possible without a major loss in PCE.[7]
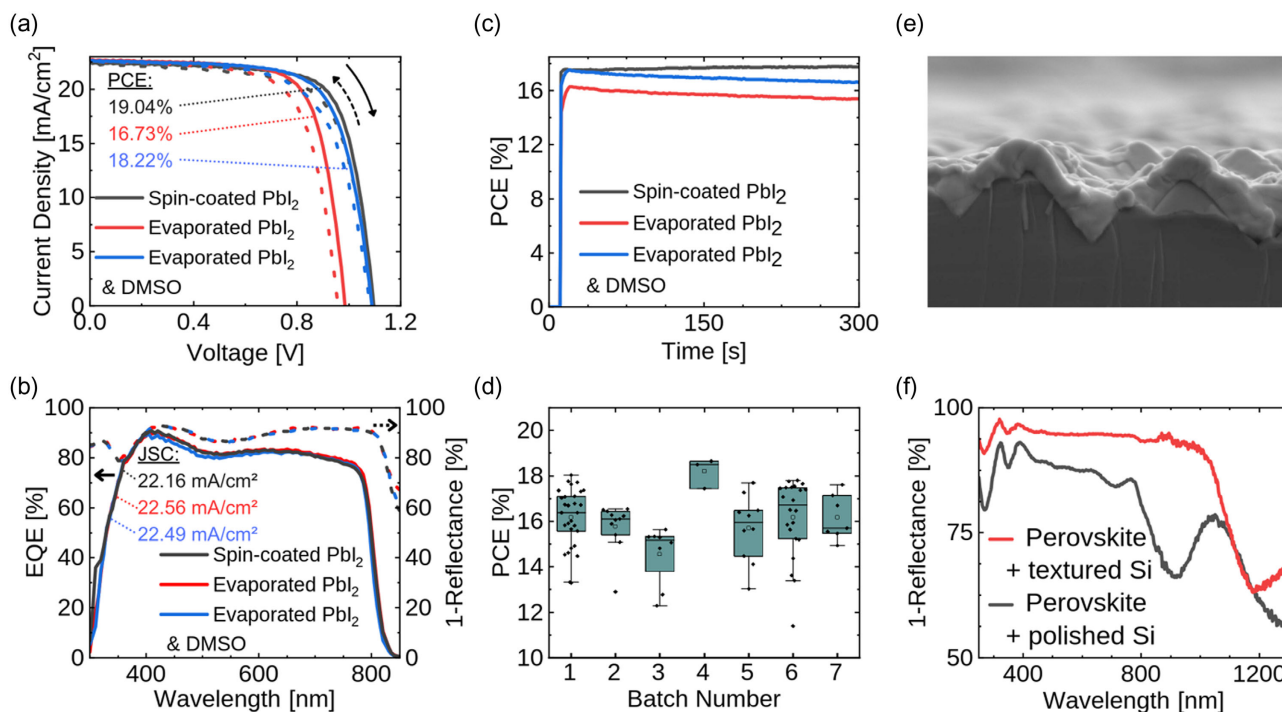

Figure 6. a) J–V curves, b) EQEs, and c) MPP tracking of the champions devices produced on a spin-coated and an evaporated lead iodide thin film, as well as on a DMSO-vapor-treated evaporated lead iodide thin film. Figure S8, Supporting Information, shows the integrated current densities that belong to the EQEs in b). d) The PCE reproducibility of spin-coated lead iodide based PSCs over seven consecutive batches and e,f) the possibility of coating textured devices with this process. Devices manufactured with slightly changed parameters (n-butanol to IPA ratio within the ink) are marked with *.

Maximum power point (MPP) tracking over 5 min shows a stable power output of over 17% PCE for the PSC based on a spin-coated lead iodide thin film while the PSCs based on an evaporated lead iodide thin film start on 16% PCE (without DMSO) and 17% PCE (with DMSO) and decrease by 1% respectively (Figure 6b). A second 10 min long MPP tracking shows that the evaporated PSC also reaches a stable power output but on a lower PCE (Figure S11, Supporting Information). During the second MPP tracking, the PCE of over 17% for the PSC based on a spin-coated lead iodide thin film remained, while the PSC based on a DMSO-vapor-treated evaporated lead iodide thin film demonstrated a PCE of over 15.5%. Given that the hysteresis of the PSC based on DMSO-vapor-treated evaporated lead iodide is slightly higher than that of the PSC based on spin-coated lead iodide, we hypothesize that difference to be the reason for the lower stabilized PCE. The batch-to-batch reproducibility of these PCEs is remarkable. Comparing seven consecutive batches (Figure 6d), high-performance PSCs are reproducibly fabricated with an average single-scan PCE of 16.24% ± 1.26% for 108 PSCs. With a standard deviation that is half as large as in the inkjet-printed one-step method, the reproducibility in the two-step method is noticeably higher.[17] Finally, the recipes that led to the production of efficient PSCs in this work are also applied to textured substrates. An SEM image of the cross-section (Figure 6e) shows that the process is suitable for producing conformal perovskite thin films. The perovskite grains extend seamlessly across the entire textured substrate. The original texture also remains untouched by the perovskite growing on it, showing a clear pyramid structure even after the perovskite deposition. To prove that the reflection-suppressing pyramid structure remains present over a large area, 1-R% measurements of the perovskite thin film on planar and textured silicon are compared (Figure 6f). The increased light coupling and the resulting reduced reflection losses are visible. Utilizing inkjet printing, this property can only be effectively enabled on a large scale through the hybrid two-step approach. This underscores the relevance of this fabrication method for achieving highly efficient, scalable, and reproducible textured tandem PSCs. It should be mentioned that this is only a proof of concept. Using this technique on textured devices is mainly beneficial for tandem solar cells based on industrial-relevant textured silicon bottom solar cells. Since the used recipe in this work has a bandgap of 1.55 eV, a further increase in bandgap up to >1.68 eV is necessary before building devices on textured substrates. However, the presented results demonstrate that transferring conformal coating through a hybrid two-step deposition method performs comparably well to the approach already presented in devices fabricated with spin-coating as the second step.[26,40] To the best of our knowledge, we show conformal perovskite growth on textures using inkjet printing for the first time.

3. Conclusion

PSCs are considered one of the most prominent contenders for the next generation of PVs. After being able to achieve high PCEs on a small scale, the reproducible and scalable production of perovskite thin films is one of the main challenges. In this study, we demonstrate a reproducible two-step perovskite deposition process with thermally evaporated inorganic lead iodide in step one and inkjet-printed organic cation precursors in step two. By changing the droplet deposition pattern, we optimize the printing parameters to obtain a homogeneous perovskite thin film. To enhance homogeneous perovskite thin-film formation, we introduce a DMSO-vapor-treatment step to the evaporated lead iodide thin film. Vapor-treated lead iodide thin films exhibit an increased absorption of the picoliter-sized inkjet droplets into the lead iodide thin film and a more uniform vertical material distribution after the ink deposition. We additionally prove that the material distribution throughout the perovskite thin film is most homogeneous when using a printing resolution that leads to the stoichiometric optimum. Optimizing the printing parameters and pretreating the evaporated lead iodide thin film, PCEs as high as 18.2% are realized on par with spin-coated counterparts. Compared to one-step inkjet-printing studies, similar average batch-to-batch single-scan PCEs with a higher reproducibility are achieved. In addition, SEM images of perovskites grown on textured silicon substrates reveal conformal coverage of textured silicon bottom solar cells. To the best of our knowledge, this is the first example showing conformal growth on textures using inkjet printing. After an additional bandgap adjustment, this work can be used to fabricate textured, high-performance perovskite silicon tandem solar cells. Due to the scalability of both evaporation and inkjet printing, this work is particularly relevant for the industrialization of perovskite silicon tandem solar cells.

4. Experimental Section

PSC Production: To produce the single-junction PSCs shown in this article, glasses coated with structured indium tin oxide (ITO) (120 nm, 15 Ω) from Luminescence Technology Corp (Lumtec) were used. In a subsequent step, these substrates were cleaned in an acetone ultrasonic bath (15 min) and then in an isopropanol ultrasonic bath (15 min). In the next step, the substrates were dried with a nitrogen gun and treated in oxygen plasma (100%, 15 min). Afterward, the hole transport layer (HTL) (2PACz, 0.5 mg ml^{-1}) from Lumtec was spin-coated onto the substrates. It was dissolved in ethanol 1 week before use and mixed in an ultrasonic bath (60 min) right after production and right before using it. The 2PACz (80 µL) solution was spin-coated onto the washed substrates within a nitrogen-filled glove box. The spin-coater settings were 3000 rpm with a starting acceleration of 1000 rpm s^{-1} and a total spin-coating time of 30 s. After spin-coating, the substrates were placed on a hot plate (100 °C, 10 min). Subsequently, the substrates were spin-coated with ethanol (80 µL) using the same spin-coating parameters. Afterward, the samples were once again placed on a hot plate (100 °C, 10 min). After the HTL deposition, various lead iodide cesium iodide thin films were deposited on the HTLs. In the following process, a distinction must be made between the deposition processes spin-coating, and thermal evaporation. The spin-coated inorganic thin films were fabricated using lead iodide (657 mg mL^{-1}) and cesium iodide (58.5 mg mL^{-1}) dissolved in a 9:1 ratio of DMF to DMSO. To dissolve the materials, the mixture was heated up on a hot plate (130 °C, 30 min) and mixed with a subsequent shaking step using a vortex shaker. After the solution cooled down to room temperature, it was spin-coated (60 µL) onto the HTL. Hereby 2000 rpm with a starting acceleration of 1500 rpm s^{-1} and a total spin-coating time of 30 s were used. The final thin film was then annealed on a hot plate (70 °C, 1 min). For the evaporated lead iodide thin film, no cesium was used, since the co-evaporation technique is more difficult to reproduce. The HTL-coated substrates were loaded into a CreaPhys evaporation system. Subsequently, lead iodide (300 nm, 1 Å s^{-1}) was evaporated. The standard recipe for the printed organic cation precursor used in this work

contains 60 mg mL^{-1} FAI, 6 mg mL^{-1} MABr, and 6 mg mL^{-1} MACl dissolved using a 9:1 ratio of n-butanol to IPA. A vortex shaker was used to dissolve the material. This ink results in the perovskite composition Cs$_{0.05}$MA$_{0.28}$FA$_{0.67}$Pb(Br$_{0.03}$Cl$_{0.06}$I$_{0.91}$)$_3$. To determine the composition, the perovskite stoichiometry was presupposed to be ABX$_3$. Since all lead iodide was applied in the first step and for the chosen recipe only Pb was occupying the B site of the perovskite, the amount of moles corresponding to 100% could be determined. When using spin-coating for the first step, the molarity of the solvent was used to determine the mole equivalent to 100%. In the case of thermally evaporated lead iodide, a void-free lead iodide thin film was assumed. With the known density of pristine PbI$_2$ (6.16 g cm^{-3}) and the height of the deposited lead iodide thin film (300 nm), the moles corresponding to 100% were calculated. Using the known mass ratios and the molar masses of the organic salts, the molar ratios of the introduced material classes (FA, MA, Cs) that occupy the A site were calculated. Similarly, the molar ratios of the material classes that occupy the X site (I, Br, Cl) were determined. For inkjet printing, a Pixdro LP50 inkjet printer by SÜSS equipped with a Sapphire QS-256/10 AAA print head (10 pL) from SÜSS was used. By controlling the print head with a wave function that has the following parameters: width = 9 µs, space = 5.7 µs, level = 45.88 V, and rise = fall = 64.7 V µs^{-1}, an average droplet size of 10 pL was achieved. Just before printing, the lead iodide (and cesium iodide) thin films were ejected from the nitrogen atmosphere. As described in the results section, both SS$_V$ (in print head travel direction) and SS$_H$ (perpendicular to the print head travel direction) were varied. In addition, parts of the PSCs were printed with the print head angled (angled) and not angled (native) toward the printing direction. On average across all batches, the best results were achieved for evaporated and spin-coated PSCs using 1000 DPI. After printing the organic cation precursor, the PSCs were annealed in an ambient atmosphere (20 °C, 40–45% relative humidity). To do so, the PSCs were placed on a hot plate (150 °C, 15 min). The PSCs were then brought back into a nitrogen glove box. Subsequently, a passivation layer (lithium fluoride, 1 nm, 0.2 Å s^{-1}), the electron transport layer (C$_{60}$, 20 nm, 0.2 Å s^{-1}), and a buffer layer (Bathocuproine, 3,5 nm, 0.2 Å s^{-1}) were vapor deposited in a thermal evaporator from Angstrom Engineering Inc. After the evaporation step, the ITO contacts were exposed again by scratching them free using a scalpel. Finally, silver (100 nm, 0.5 Å s^{-1}) was deposited through a mask by thermal evaporation. For that, an evaporator by VacTec (COAT340) was used. Throughout the texture of the ITO thin film and the silver contacts, four PSCs (10.5 mm^2) were created on each substrate.

J–V Measurement: For measuring the PSCs characteristics, a xenon-lamp-based solar simulator (Newport Oriel Sol3A) with an AM1.5 G spectrum (1000 W m^{-2}) was calibrated using a certified silicon solar cell (Newport) equipped with a KG5 band-pass filter. Subsequently, the PSCs were measured in backward and forward directions with a step size of 10 mV. All cells were measured from −0.2 to 1.2 V with a scanning rate of 0.6 V s^{-1} using a Keithley 2401 source measurement unit. During the measurement, the temperature of the PSCs was held at 25 °C with a microcontroller-adjusted Peltier element. The MPP was tracked by using a perturb-and-observe method. The measurements were performed in a nitrogen glove box.

External Quantum Efficiency Measurement: The EQEs were measured using a PVE300 PV QE system (Bentham EQE system). For calibration, a silicon reference solar cell was used. All measurements were done using a 0.74 mm^2 illumination spot with a chopping frequency between 560–590 Hz and an integration time of 500 ms. The measurement step size was 5 nm. The measurements were performed in a nitrogen glove box.

Reflectance Measurement: Reflectance spectra of the perovskite thin films were measured using a PerkinElmer Lambda1050 spectrophotometry setup equipped with a double-monochromator and a modulated source. A chopper frequency of 46 Hz was applied.

Time-Resolved Microscopy Images: Time-resolved microscopy images were recorded using an optical contact angle and drop contour analyzer (DataPhysics Instruments GmbH, OCA 200) applied with the PicoDrop kit. Hereby, cartridges which jet 30 pL droplets were used.

XRD Measurements: The crystal structure of the perovskite layers was carried out utilizing XRD (Bruker D2 Phaser system) with Cu-Kα radiation (λ = 1.5405 Å) in Bragg–Brentano configuration using a LynxEye detector. The XRD was taken from the perovskite layer deposited on the ITO/2PACz substrate to obtain the same perovskite nucleation, and crystallization as in the solar cells.

ToF–SIMS Measurements: ToF–SIMS was performed on a TOF.SIMS5 instrument (ION-TOF). The spectrometer had a Bi cluster primary ion source and a reflectron-type ToF analyzer. A dual-beam analysis was performed in interlaced mode to enable depth profiling. The sputter gun operated with Ar$_{1500}$ cluster ions at 10 keV and scanned over a field of view of 750 × 750 µm^2 (target current 10 nA). This gun was used to erode the sample, whereas the primary ion source (25 keV Bi$_3$$^+$) was scanned over a concentric field of 500 × 500 µm^2 (128 × 128 data points). The omnipresent C$^+$, CH$^+$, CH$_2$$^+$, CH$_3$$^+$, Na$^+$, K$^+$, ^{113}In$^+$, and ^{204}Pb$^+$ signals or the Cl$^-$, PO$_2$$^-$, ^{113}InO$^-$, In$_2O_2$$^-$, and PbI$_2$$^-$ peaks were used to calibrate the spectra. Based on these datasets, the chemical assignments for characteristic fragments were determined. For data visualization, secondary ion intensities were rendered to 2D depth profile images.

SEM: SEM analysis was carried out in an SEM (Zeiss LEO1530) with an in-lens detector and an aperture size of 20–30 µm. The applied acceleration voltages for surface and cross-sectional analysis ranged between 3 and 5 kV.

Microscopy: Microscope images were taken with a Zeiss Axioplan 2 imaging.

Profilometry: The thickness of the perovskite films was measured using a Bruker Dektak XT profilometer.

Photoluminescence Mapping: The photoluminescence images were recorded using a self-made measurement setup described in more detail in ref. [13].

Statistical Representation: In boxplots, symbols serve to visually represent key statistical insights. The colored blocks represent the interquartile range (IQR), spanning from the 25th to the 75th percentile of the data. A vertical line extends to 1.5 times the IQR, aiding in identifying potential outliers. The horizontal line denotes the median, while the hollow square signifies the mean. Data points and outliers that are falling outside the expected range are depicted as rhombuses.

Supporting Information

Supporting Information is available from the Wiley Online Library or from the author.

Acknowledgements

Conflict of Interest

The authors declare no conflict of interest.

Data Availability Statement

The data that support the findings of this study are available from the corresponding author upon reasonable request.

Keywords

hybrid deposition, inkjet-printing, perovskite, solar cell, two-step deposition

[1] IPCC, in *Contribution of Working Groups I, II and III to the Sixth Assessment Report of the Intergovernmental Panel on Climate Change*, Core Writing Team (Eds: H. Lee and J. Romero), IPCC, Geneva, Switzerland **2023**, pp. 35–115.

[2] Clarke, L., Y.-M. Wei, A. De La Vega Navarro, A. Garg, A. N. Hahmann, S. Khennas, I. M. L. Azevedo, A. Löschel, A. K. Singh, L. Steg, G. Strbac, K. Wada, In *IPCC, 2022: Climate Change 2022: Contribution of Working Group III to the Sixth Assessment Report of the Intergovernmental Panel on Climate Change* (Eds: P.R. Shukla, J. Skea, R. Slade, A. Al Khourdajie, R. van Diemen, D. McCollum, M. Pathak, S. Some, P. Vyas, R. Fradera, M. Belkacemi, A. Hasija, G. Lisboa, S. Luz, J. Malley), Cambridge University Press, Cambridge, UK and New York, NY, USA **2022**, p. 632.

[3] H. Zhang, X. Ji, H. Yao, Q. Fan, B. Yu, J. Li, *Solar Energy* **2022**, *233*, 421.

[4] http://NREL.goNREL, Best Research-Cell Efficiencies. https://www.nrel.gov/pv/assets/pdfs/best-research-cell-efficiencies.pdf (accessed: February 2023).

[5] S. L. Hamukwaya, H. Hao, Z. Zhao, J. Dong, T. Zhong, J. Xing, L. Hao, M. M. Mashingaidze, *Coatings* **2022**, *12*, 252.

[6] R. Wang, M. Mujahid, Y. Duan, Z. Wang, J. Xue, Y. Yang, *Adv. Funct. Mater.* **2019**, *29*, 1808843.

[7] R. Pappenberger, A. Diercks, J. Petry, S. Moghadamzadeh, P. Fassl, U. W. Paetzold, *Adv. Funct. Mater.* **2023**, *34*, 2311424.

[8] E. L. Unger, L. Kegelmann, K. Suchan, D. Sörell, L. Korte, S. Albrecht, *J. Mater. Chem. A* **2017**, *5*, 11401.

[9] D. Li, D. Zhang, K.-S. Lim, Y. Hu, Y. Rong, A. Mei, N.-G. Park, H. Han, *Adv. Funct. Mater.* **2021**, *31*, 2008621.

[10] I. Susic, L. Gil-Escrig, F. Palazon, M. Sessolo, H. J. Bolink, *ACS Energy Lett.* **2022**, *7*, 1355.

[11] D. B. Ritzer, T. Abzieher, A. Basibüyük, T. Feeny, F. Laufer, S. Ternes, B. S. Richards, S. Bergfeld, U. W. Paetzold, *Prog. Photovolt. Res. Appl.* **2022**, *30*, 360.

[12] B. Abdollahi Nejand, D. B. Ritzer, H. Hu, F. Schackmar, S. Moghadamzadeh, T. Feeny, R. Singh, F. Laufer, R. Schmager, R. Azmi, M. Kaiser, T. Abzieher, S. Gharibzadeh, E. Ahlswede, U. Lemmer, B. S. Richards, U. W., Paetzold, *Nat. Energy* **2022**, *7*, 620.

[13] F. Laufer, S. Ziegler, F. Schackmar, E. A. Moreno Viteri, M. Götz, C. Debus, F. Isensee, U. W. Paetzold, *Sol. RRL* **2023**, *7*, 2201114.

[14] K. Geistert, S. Ternes, D. B. Ritzer, U. W. Paetzold, *ACS Appl. Mater. Interfaces* **2023**, *15*, 52519.

[15] S. Uličná, B. Dou, D. H. Kim, K. Zhu, J. M. Walls, J. W. Bowers, M. F. A. van Hest, *ACS Appl. Energy Mater.* **2018**, *1*, 1853.

[16] B. Tyagi, N. Kumar, H. B. Lee, M. M. Ovhal, V. V. Satale, A. Mohamed, D. H. Kim, J. W. Kang, *Small Methods* **2023**, *8*, 2300237.

[17] H. Eggers, F. Schackmar, T. Abzieher, Q. Sun, U. Lemmer, Y. Vaynzof, B. S. Richards, G. Hernandez-Sosa, U. W. Paetzold, *Adv. Energy Mater.* **2020**, *10*, 1903184.

[18] J. Zimmermann, S. Schlisske, M. Held, J-N. Tisserant, L. Porcarelli, A. Sanchez-Sanchez, D. Mecerreyes, G. Hernandez-Sosa, *Adv. Mat. Tech.* **2019**, *4*, 1800641.

[19] M. Hösel, R.R. Søndergaard, D. Angmo, F. C. Krebs, *Adv. Eng. Mater.* **2013**, *15*, 995.

[20] Inuru GmbH, The Dragon Factory: World's First Low Cost OLED Production, https://www.inuru.com (accessed: January 2024)

[21] I. A. Howard, T. Abzieher, I. M. Hossain, H. Eggers, F. Schackmar, S. Ternes, B. S. Richards, U. Lemmer, U. W. Paetzold, *Adv. Mat.* **2019**, *10*, 1806702.

[22] Z. Li, P. Li, G. Chen, Y. Cheng, *ACS Appl. Mater. Interfaces* **2020**, *12*, 39082.

[23] S. Siegrist, S.-C. Yang, E. Gilshtein, X. Sun, A. N. Tiwari, F Fu, *Chem. A. Mater.* **2021**, *9*, 26680.

[24] K. Liang, D. B. Mitzi, M.T. Prikas, *Chem. Mater.* **1998**, *10*, 403.

[25] J. Burschka, N. Pellet, S-J. Moon, R. Humphry-Baker, P. Gao, M. K. Nazeeruddin, M. Grätzel, *Nature* **2013**, *499*, 316.

[26] X. Y. Chin, D. Turkay, J. A. Steele, S. Tabean, S. Eswara, M. Mensi, P. Fiala, C. M. Wolff, A. Paracchino, K. Artuk, D. Jacobs, Q. Guesnay, F. Sahli, G. Andreatta, B. Mathieu, W. Jeangros, C. Ballif, *Science* **2013**, *381*, 59.

[27] W. Soltanpoor, C. Dreessen, M. C. Sahiner, I. Susic, A. Z. Afshord, V. S. Chirvony, P. P. Boix, G. Gunbas, S. Yerci, H. J. Bolink, *ACS Appl. Energy Mater.* **2020**, *3*, 8257.

[28] O. Schultz-Wittmann, S. Patricia, E-R. Oussama, R. Efinger, Ö. S. Kabakli, H. Maryamsadat, M. M. Kaitlyn, O. Fischer, A. J. Bett, D. Erath, S. Pingel, U. Heitmann, Z. Kiaee, M. Kohlstädt, B. Kore, H. Nagel, M. Schubert, M. Bivour, J. C. Goldschmidt, A. J. Borchert, S. Glunz, *Energy Convers.* **2022**, *31*, 354.

[29] Z. Xiao, Q. Dong, C. Bi, Y. Shao, Y. Yuan, J. Huang, *Adv. Mater.* **2014**, *26*, 6503.

[30] H. Chen, X. Ding, P. Xu, T. Hayat, A. Alsaedi, J. Yao, Y. Ding, S. Dai, *ACS Appl. Mater. Interfaces* **2018**, *10*, 1781.

[31] V. S. Nguyen, I. Zimmermann, E. Grépin, K. Medjoubi, S. Jutteau, F. Donsanti, E. Bruhat, A. Duchatelet, S. Berson, J. Rousset, *Mater. Sci. Semicond. Process.* **2023**, *158*, 107358.

[32] J. Fang, D. Lin, W. Huang, X. Wang, H. Li, S. Li, G. Xie, D. Wang, L. Qiu, *J. Alloys Compd.* **2023**, *955*, 170255.

[33] T. Liu, Q. Hu, J. Wu, K. Chen, L. Zhao, F. Liu, C. Wang, H. Lu, S. Jia, T. Russell, R. Zhu, Q. Gong, *Adv. Energy Mater.* **2016**, *6*, 1501890.

[34] R. D. Deegan, O. Bakajin, T. F. Dupont, G. Huber, S. R. Nagel, T. A. Witten, *Phys. Rev. E: Stat. Phys., Plasmas, Fluids, Relat. Interdisc. Top.* **2000**, *62*, 756.

[35] X. Fanton, A. M. Cazabat, *Langmuir* **1998**, *14*, 2554.

[36] G. Li, X. Zou, J. Cheng, D. Chen, Y. Yao, C. Chang, X. Yu, Z. Zhou, J. Wang, B. Liu, *Molecules* **2020**, *25*, 732.

[37] N. Cheng, Z. Yu, W. Li, B. Lei, W. Zi, Z. Xiao, Z. Zhao, P-A. Zong, *ACS Appl. Energy Mater.* **2022**, *5*, 15385.

[38] A. Farag, R. Schmager, P. Fassl, P. Noack, B. Wattenberg, T. Dippell, U. W. Paetzold, *ACS Appl. Energy Mater.* **2022**, *5*, 6700.

[39] F. Liu, Q. Dong, M. K. Wong, A. B. Djurišić, A. Ng, Z. Ren, Q. Shen, C. Surya, W. K. Chan, J. Wang, A. M. C. Ng, C. Liao, H. Li, K. Shih, C. Wei, H. Su, J. Dai, *Adv. Energy Mater.* **2016**, *6*, 1502206.

[40] J. Werner, F. Sahli, F. Fu, J. J. D. Leon, A. Walter, B. A. Kamino, B. Niesen, S. Nicolay, W. Jeangros, C. Ballif, *ACS Energy Lett.* **2018**, *3*, 2052.